AGU PUBLICATIONS

JGR

Journal of Geophysical Research: Oceans

RESEARCH ARTICLE

10.1002/2013JC009459

Key Points:
- Autonomous sea ice albedo setup was developed and deployed in high Arctic
- Strong influence of sky and surface conditions variation on absorbed energy
- Solar heat could explain all of the observed snow and sea ice melt in 2012

Correspondence to:
C. Wang,
caixin.wang@npolar.no

Citation:
Wang, C., M. A. Granskog, S. Gerland, S. R. Hudson, D. K. Perovich, M. Nicolaus, T. I. Karlsen, K. Fossan, and M. Bratrein (2014), Autonomous observations of solar energy partitioning in first-year sea ice in the Arctic Basin, *J. Geophys. Res. Oceans*, *119*, 2066–2080, doi:10.1002/2013JC009459.

Received 23 SEP 2013
Accepted 28 FEB 2014
Accepted article online 7 MAR 2014
Published online 21 MAR 2014

Autonomous observations of solar energy partitioning in first-year sea ice in the Arctic Basin

Caixin Wang[1], Mats A. Granskog[1], Sebastian Gerland[1], Stephen R. Hudson[1], Donald K. Perovich[2], Marcel Nicolaus[3], Tor Ivan Karlsen[1], Kristen Fossan[1], and Marius Bratrein[1]

[1]Norwegian Polar Institute, Fram Centre, Tromsø, Norway, [2]Cold Regions Research and Engineering Laboratory, Hanover, New Hampshire, USA, [3]Alfred-Wegener-Institut, Helmholtz-Zentrum für Polar- und Meeresforschung, Bremerhaven, Germany

Abstract A Spectral Radiation Buoy (SRB) was developed to autonomously measure the spectral incident, reflected, and transmitted spectral solar radiation (350–800 nm) above and below sea ice. The SRB was deployed on drifting first-year sea ice near the North Pole in mid-April 2012, together with velocity and ice mass balance buoys. The buoys drifted southward and reached Fram Strait after approximately 7 months, covering a complete melt season. At the SRB site, snowmelt started on 10 June, and had completely disappeared by 14 July. Surface albedo was above 0.85 until snowmelt onset and decreased rapidly with the progression of snowmelt. Albedo was lowest on 14 July, when the observed surface was likely a mixture of bare ice and melt pond(s). The transmitted irradiance measured under the ice was largest in July, with a monthly average of 20 W m^{-2}, compared to $<$0.3 W m^{-2} premelt. Under-ice irradiance peaked on 19–20 July, with a daily average around 35 W m^{-2}. From mid-April to mid-September, the solar energy transmitted through the ice into the ocean contributed about two-thirds of the energy required for the observed bottom melt (0.49 m). The energy absorbed by the ice after snowmelt was enough to melt an additional 0.1 m of ice. Solar energy incident on open water and melt ponds provided significant additional heating, indicating solar heating could explain all of the observed bottom melt in this region in summer 2012.

1. Introduction

The Arctic sea ice cover has undergone tremendous changes in recent years. Summer extent has declined [*Comiso et al*., 2008], thickness has decreased [*Haas et al*., 2008; *Kwok and Rothrock*, 2009; *Hansen et al*., 2013; *Laxon et al*., 2013], and the ice pack has become younger [*Nghiem et al*., 2007; *Maslanik et al*., 2007, 2011]. The ongoing shift from a largely perennial Arctic ice pack to a thinner seasonal one has resulted in a decrease in surface albedo and an increase in light transmission to the upper ocean [*Perovich et al*., 2011a; *Nicolaus et al*., 2012; *Perovich and Polashenski*, 2012; *Hudson et al*., 2013], such that more energy is deposited into the Arctic Ocean [*Perovich et al*., 2007; *Nicolaus et al*., 2012; *Hudson et al*., 2013].

Surface albedo plays a key role in the amount of energy that is deposited into the snow and ice cover and the surface ocean. Sea ice surface albedo is dependent on various factors: snow grain size [*Grenfell and Perovich*, 1984; *Warren*, 1982], snow depth and ice thickness [*Brandt et al*., 2005; *Grenfell and Maykut*, 1977], extent and depth of melt ponds [*Hanesiak et al*., 2001; *Perovich et al*., 2002], and atmospheric conditions. The surface albedo of sea ice has been measured in different seasons and regions in the Arctic [e.g., *Grenfell and Maykut*, 1977; *Perovich et al*., 2002; *Perovich and Polashenski*, 2012; *Hudson et al*., 2012]. However, available data are mainly from manual and discontinuous observations.

The availability of sunlight beneath the ice is of importance for the Arctic marine ecosystem [e.g., *Perovich et al*., 1993; *Arrigo et al*., 2012], upper ocean heating [*Perovich*, 2005; *Itoh et al*., 2011], and subsequent bottom ice melt [*Perovich et al*., 2011b; *Hudson et al*., 2013]. Observations of solar radiation transmittance through Arctic sea ice have been conducted [e.g., *Perovich et al*., 1998; *Light et al*., 2008; *Nicolaus et al*., 2010a ; *Ehn et al*., 2011; *Nicolaus et al*., 2012], and some from the thinner Arctic ice pack have recently emerged [*Frey et al*., 2011; *Nicolaus et al*., 2012; *Hudson et al*., 2013], showcasing how different the thinner ice regime is in contrast to the earlier thicker ice pack. However, observations are sporadic in space and time. Much of the knowledge about the optical properties of sea ice is still from thicker multiyear ice, and observations of complete seasonal cycles in the high Arctic are rare [*Nicolaus et al*., 2010a] due to the

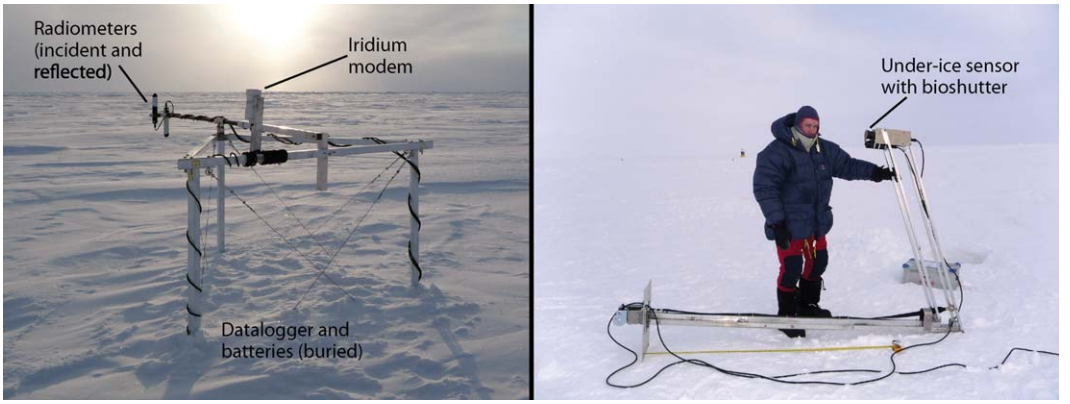

Figure 1. (a) The surface frame of the Spectral Radiation Buoy after final setup and (b) the under-ice arm of the SRB before final installation.

remoteness, harsh conditions, and logistical challenges. Observations of surface and bottom melt [*Perovich et al*., 2008; *Hudson et al*., 2013] indicate the importance of solar radiation to sea ice mass balance; however, there are very little radiation data from the high Arctic, especially from the new thinner ice regime.

To continuously observe solar radiation above and below the sea ice, an integrated instrument setup was developed for the drift of the schooner *Tara* during the International Polar Year 2007–2008 [*Nicolaus et al*., 2010b]. The setup with three spectroradiometers (two in air and one under the ice) was deployed near *Tara* and regularly maintained by the *Tara* team. It proved suitable for autonomous and long-term observations over and under sea ice in cold and harsh conditions. However, this system had no satellite data transfer, requiring manual data retrieval. A new, fully autonomous setup was developed and deployed, and here we report the results of its first deployment, presenting the seasonal changes in solar radiation and its partitioning in first-year sea ice in the high Arctic.

2. Materials and Methods

2.1. Spectral Radiation Buoy (SRB) Setup

The SRB is an improvement of the setup used on the *Tara* drift [*Nicolaus et al*., 2010a]. In addition to three radiometers and one data logger, it also includes a bioshutter on the under-ice radiometer and an Iridium modem to transmit data in near real time (Figure 1).

The setup uses three HyperOCR radiometers (Satlantic, Inc.), which have a history of successfully measuring spectral irradiance in marine environments [e.g., *Chang and Dickey*, 2004; *Ehn et al*., 2011]. The radiometers cover a wavelength range of 350–800 nm, and are separately calibrated for measurements in air and water. The sensors sample data every 3.3 nm, with a 10 nm spectral resolution. The radiometers also have built-in two-axis tilt meters.

2.1.1. Surface Unit of the SRB

The surface unit of the SRB includes two spectroradiometers, a MELO-RL Iridium modem, a measurement control unit and data logger (Satlantic STOR-X), a lithium-battery pack, and a mounting frame. The frame was designed to be robust and stable and to freeze into the ice after installation (Figure 1a). The radiometers are mounted on an arm extending 1.65 m from one vertex of the frame to measure spectral incident and reflected irradiances.

2.1.2. Under-Ice Part of the SRB

The under-ice part of the SRB is not mechanically connected to the surface frame; it includes an upward-looking spectroradiometer mounted on an adjustable under-ice arm (Figure 1b). The radiometer measures transmitted irradiance under the ice. It is connected with a cable to the STOR-X unit.

Table 1. Summary of Data Sets at the SRB Site

Instrument	Time and Duration	Observation Parameters
SRB	13 Apr to 13 Sep 2012	Hourly spectral incident and reflected irradiances
	13 Apr to 4 Oct 2012	Hourly spectral transmitted irradiances, tilt angles, Iridium position, battery voltage
IMB (ID: 2012C)	17 Apr to 13 Oct 2012	Distance to snow surface every four hours; air, snow, ice, and under-ice water temperature, air pressure, and Iridium position every hour
SVP	13 Apr 2012 to Jan 2013	Hourly GPS position and surface temperature
	15 Apr 2012	Manual snow and ice thickness measurements; vertical salinity profile, snow and seawater samples for salinity and $\delta^{18}O$ measurement

This radiometer is fitted with a bioshutter that has a copper plate to cover the sensor, opening to expose the sensor surface only when measurements are taken. While the shutter is closed, the under-ice sensor is covered to prevent biofouling or accumulation of particles or organic material falling onto the sensor. The arm and sensor holder are designed so that the sensor always points up, independent of the angle of the arm. During installation, the arm is straight for fitting through the drill hole, and then the angle of the arm is adjusted into the L-shape using a small winch. After deployment, the under-ice sensor is about 1.5 m from the drill hole through which it is installed.

2.2. SRB Deployment in the Arctic Basin and Recovery in Fram Strait

2.2.1. Deployment at Barneo

The Russian ice camp Barneo (http://www.Barneo.ru) was used as a platform to deploy the SRB, due to its location in the central Arctic and operation time (April) before snowmelt onset. The SRB, a MetOcean Ice Mass Balance buoy (IMB) [*Richter-Menge et al*., 2006], and a Surface Velocity Program buoy (SVP; MetOcean) were deployed within 30 m of each other. The deployment site was 250 m away from the main Barneo camp, on first-year ice that had a modal snow thickness of 0.375 m (based on 188 independent direct snow thickness measurements along transects within 1 km of the site). The majority of the snow thicknesses were between 0.25 and 0.55 m.

The SRB was deployed on 13 April 2012. The radiometers were 1.0 m above the snow surface and, at installation, were south of the frame. The under-ice part was deployed through an auger hole (250 mm diameter). The sensor was positioned south of the hole, about 4 m away from the sensors above the surface, and, at the time of installation, it was 0.5 m below the ice bottom to allow for additional ice growth during the observation period. The surface support for the under-ice arm was fixed to the ice with two ice screws. The cable from the under-ice sensor to the data logger was buried under the snow. After deployment, the surface was restored as well as possible (Figure 1), and the auger hole was left to freeze.

Next to the SRB, an IMB buoy (number 2012C) was deployed on 17 April 2012. It was used to highlight key transitions in the ice cover; for example, when the snow began to melt, when the snow was completely gone, when ice surface started to melt and when freezeup occurred, and to get an estimate of the amount of surface and bottom melting. The IMB included two acoustic rangefinders to determine ice surface and bottom locations, a thermistor chain through the snow and sea ice, an air temperature sensor, a barometer, a Campbell Scientific data logger, and an Iridium modem. Unfortunately, the under-ice acoustic rangefinder did not function. To complement the information on surface ablation, the ablation stakes installed in the view of UW webcams were used.

The SVP buoy was deployed on 16 April 2012. Its GPS receiver provided the accurate position of the ice floe, complementing SRB and IMB positions from Iridium.

2.2.2. In Situ Measurements

Snow thickness, ice thickness, and freeboard were measured at the SRB and IMB sites to get initial conditions. Three ice cores were collected at the SRB site. One was for salinity measurement in the field right after the ice core was collected, and the remaining cores were sealed and shipped to labs for measuring oxygen isotopic composition ($\delta^{18}O$). A summary of the measurements is shown in Table 1.

2.2.3. Other Deployments at Barneo

In addition to the installations at the SRB site, several other instruments were deployed in April on a neighboring multiyear ice floe, which was 2.74 m thick, with 0.3 m of snow. These included a similar IMB buoy (number 2012B; the above ice rangefinder stopped working on 27 June 2012) from Cold Regions Research

and Engineering Laboratory (CRREL), an Ice-tethered profiler (ITP63) from Woods Hole Oceanographic Institution (WHOI), two web cameras (1 and 2) from University of Washington (UW), one SAMS (Scottish Association for Marine Science) IMB buoy [*Jackson et al*., 2013] and a Acoustic Ice Tethered Platform (AITP) from Université Pierre et Marie Curie (UPMC), and an O-buoy from Bigelow Laboratories. Webcams recorded the surface development and sky conditions from 22 April onward. Ablation stakes were installed in the view of UW webcams. Our SRB buoy was in the far view of webcam 1. Therefore, we could follow in real time the evolution of surface conditions on the ice floe.

2.2.4. SRB Recovery in Fram Strait

Supported by SVP positions, the research vessel *Lance* found the Barneo ice floe at 79°40′N in the Fram Strait on 4 October 2012 (see drift Figure 2a). When it was found, the floe had broken into smaller floes. Our instruments were on two neighboring ice floes (a few meters apart), one with the SRB, the other with SVP and IMB 2012C. The conditions made it infeasible to make any measurements of the snow and ice properties during recovery. The SRB frame was intact, but the arm holding the two above-ice sensors was broken, likely by a polar bear when it visited the ice floe on 14 September as recorded by the tilt data and photos. All parts of the SRB were recovered except the under-ice sensor and arm.

2.3. Data Processing

2.3.1. SRB Data Processing

Hourly SRB spectral irradiance data are stored in the data logger, and transmitted by Iridium satellite link. During the season, the SRB transferred 4406 incident, reflected, and transmitted irradiance spectra. These spectra were later corrected with measured dark currents, and processed to absolute spectral data with individual calibration files for each sensor. Under-ice data are of good quality for the entire period, but the incident and reflected data are useful only until the arm supporting the above-ice sensors was broken. Therefore, analyses are shown through 13 September, except for the transmitted fluxes.

Spectral albedo is calculated as

$$\alpha(\lambda,t)=\frac{F_R(\lambda,t)}{F_I(\lambda,t)} \tag{1}$$

and spectral transmittance is equivalent as

$$\tau(\lambda,t)=\frac{F_T(\lambda,t)}{F_I(\lambda,t)} \tag{2}$$

where F_I, F_R, and F_T are measured spectral incident, reflected, and transmitted irradiances, respectively, which vary with wavelength (λ) and time (t). It should be noted that the transmitted irradiance was measured at a distance below the ice bottom (0.5 m at deployment), and includes the effect of the water layer between the sensor and the ice bottom. Mean in-band albedo $\overline{\alpha_T}$ and transmittance $\overline{\tau_T}$ (over time and wavelength) are calculated from the integrated fluxes as

$$\overline{\alpha_T}=\frac{\int_{t1}^{t2}\int_{350}^{800}F_R(\lambda,t)d\lambda dt}{\int_{t1}^{t2}\int_{350}^{800}F_I(\lambda,t)d\lambda dt} \tag{3}$$

and

$$\overline{\tau_T}=\frac{\int_{t1}^{t2}\int_{350}^{800}F_T(\lambda,t)d\lambda dt}{\int_{t1}^{t2}\int_{350}^{800}F_I(\lambda,t)d\lambda dt} \tag{4}$$

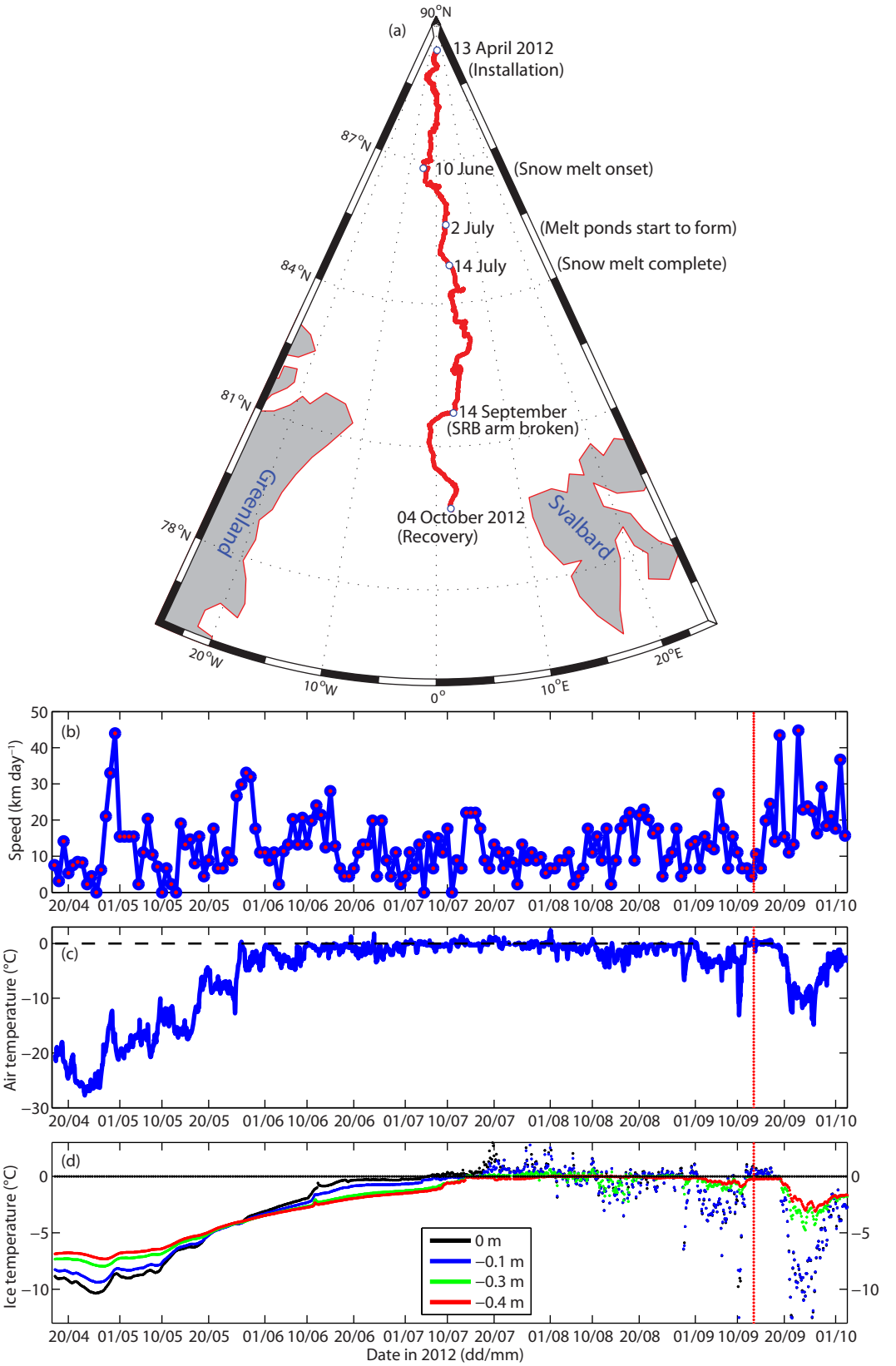

Figure 2. (a) Drift track and (b) daily drift speed of the Barneo ice floe based on SVP GPS positions, and (c) air temperature and (d) ice temperature recorded by IMB (after 6 July the ice surface melted below the upper ice thermistors). Red vertical lines indicate 14 September when the arm of the SRB was broken.

Note that the in-band quantities cover only a limited wavelength range between 350 and 800 nm. Fluxes of photosynthetically active radiation (PAR) were converted to photon flux per unit area over the wavelength range from 400 to 700 nm; these quantum fluxes were also used to calculate PAR transmittance. To examine the temporal evolution, we have calculated the means over periods covering the early (days 1–10), middle (days 11–20), and late (days 21–30/31) parts of each month, as well as monthly means.

2.3.2. IMB Data Processing

By combining information from the two IMBs at the Barneo site (IMB 2012B and 2012C), we can estimate the evolution of the snow depth and ice thickness at the SRB site, despite the failure of one rangefinder on each IMB. Distances to the snow (later ice) surface were recorded by the above ice acoustic rangefinder on IMB 2012C. Combined with our knowledge of the initial snow depth, this allows us to follow the progression of snowmelt and ice surface melt. By knowing the initial ice thickness, changes in the distance to the under-ice rangefinder can be used to derive changes at the ice bottom (growth and melt). Since the under-ice rangefinder of IMB 2012C did not work, we have used the changes observed at IMB 2012B assuming the same progression of ice bottom growth and melt at the two IMB sites [*Perovich and Richter-Menge*, 2006]. When the ice is isothermal in summer, the ice bottom melt is dominated by the ocean heat flux. Assuming a similar ocean heat flux, the difference in ice melt, irrespective of its thickness, are likely small at the IMB 2012B and 2012C since they were moving together. Altogether this gives us a good idea of the development of snow depth and ice thickness at the SRB site.

3. Results

3.1. The Barneo Ice Floe Drift

On 13 April 2012, the Barneo ice floe was in the Amundsen Basin at 89° 31′N, 4° 23′E, 55 km from the North Pole. Thereafter, it drifted southward toward Fram Strait and reached 79°40′N in the Fram Strait on 4 October 2012 (Figure 2a). The daily mean drift speed was 15 km d^{-1} (Figure 2b), with the highest speed of 45 km d^{-1} on 30 April. Based on hourly data from the SVP, the Barneo ice floe drifted 2235 km in just over 7 months, approximately twice its net displacement in that period.

3.2. Air and Ice Temperature

Figure 2c shows air temperature from mid-April to early October 2012. The air temperature was low in April (mostly <-20°C) and then increased. A temperature above 0°C was first reached on 27 May. Thereafter, it fluctuated between -5 and 0°C until 19 June, and in July and August the air temperature remained between 0 ± 2°C except between 10 and 20 August when there was a cold spell. Later on, air temperatures decreased with the exception of some intermittent periods with near zero temperatures.

The ice surface temperature (Figure 2d) shows a similar temporal variation as the air temperature from mid-April to mid-September, although the variation was less pronounced at the ice surface than in the air before 6 July, due to the attenuation effect of snow (see Figure 4) [*Perovich and Elder*, 2001]. The temperatures measured by the IMB thermistors at depths of 0, 0.1, 0.3, and 0.4 m below the ice surface (at deployment) began showing above zero temperatures and rapid fluctuation on 6 July, 14 July, 25 July, and 2 August (Figure 2d), respectively, implying when surface melt at the thermistor chain possibly reached those levels and the thermistors were in air.

3.3. Ice Properties and Surface Conditions of the Barneo Ice Floe

The ice core (length 1.35 m) collected at the SRB site had a bulk-salinity of 4.0, with a low-salinity layer of 2.0 at the surface, and salinity between 3.5 and 6.4 below 0.2 m. The low-salinity layers at the surface also had negative δ^{18}O values (not shown) that were much lower than the values in the rest of the ice core, suggesting that the top 0.2 m of the ice cover at deployment was snow ice.

The surface conditions of the ice floe captured by UW webcam 1 are shown in Figure 3. Within the field of webcam view, the ice floe was completely covered by snow until late June (Figure 3b). From 2 July, melt ponds started to form (Figure 3c) and developed further (Figure 3d), including deepening (Figure 3e), and increasing in area (Figure 3f). The pond area reached a maximum extent in mid-July. Pond drainage after mid-July (Figure 3g) decreased the pond area, making the bare ice surface drier and whiter. Ponds then remained steady (Figure 3h) until 18 August (not shown). With snowfall on 19 August, melt ponds started to refreeze (Figures 3i and 3j). By 21 September (not shown), the surface was completely covered by snow.

Figure 3. Surface evolution recorded at times indicated in the photographs by webcam 1 from University of Washington (UW) in 2012 (source: http://psc.apl.washington.edu/northpole/NPEO2012/WEBCAM1/ARCHIVE/). The rectangle in Figure 3a indicates the location of the SRB. The rectangle in Figure 3f indicates the locations of ablation stakes in the far view.

Based on the webcam photos, the maximum fraction of melt ponds was estimated to be about 25% (see Figure 3f) in the view of the camera. This is comparable to the pond fraction in the Arctic Basin during the *Tara* drift in the study of *Sankelo et al*. [2010] and in late July 2012 [*Hudson et al*., 2013], but is less than the fraction observed by *Nicolaus et al*. [2012]. Since the SRB was too far from the webcam, we cannot use the

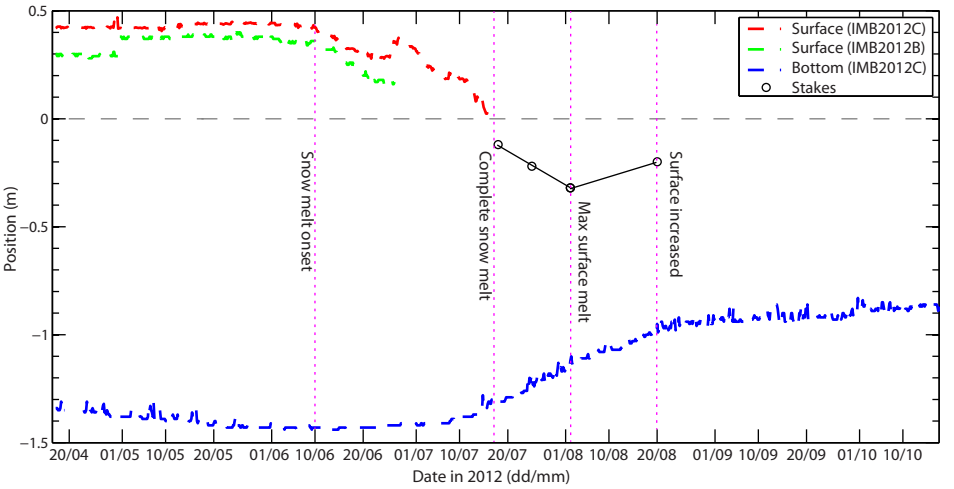

Figure 4. IMB-derived surface positions and bottom position (assuming the growth and decay of ice at the ice bottom was same at IMB 2012B and IMB 2012C), and surface evolution estimated from ablation stakes after complete snowmelt (solid black line). Vertical lines indicate the dates of snowmelt onset (10 June), complete snowmelt (17 July), maximum surface melt (2 August), and surface rebound (20 August). Zero level indicates the initial snow-ice interface at deployment.

webcam to identify the surface type below the radiometers. As discussed in section 4, we believe, based on the spectra, that the downward looking radiometer was seeing a mix of bare ice and melt pond in mid-July to late July.

3.4. Snow Depth and Ice Thickness Evolution

In April, the snow depth and ice thickness varied slightly at the different locations around the SRB site. The initial snow depth and ice thickness was 0.49 and 1.20 m, respectively, at the SRB site, with a freeboard of −0.06 m. At the IMB 2012C site, they were 0.43 and 1.24 m at the thermistor chain, and 0.42 and 1.34 m at the sonar mast, with a freeboard of 0 and 0.03 m, respectively.

The surface at the IMB site was covered by snow in April, May, and June (Figure 4). Snowmelt started around 10 June at the two IMBs; before then snow depth had not changed much. The sudden increase of snow depth at IMB 2012B before 1 May was due to snow drift, as the drift speed of the ice floe was maximum at that time (Figure 2b) and the appearance of snow dunes in the view of UW webcams. After 10 June, snow depth decreased, interrupted by the occasional snowfall. From 30 June onward, snow depth decreased steadily, and by 17 July all snow had disappeared at IMB 2012C (Figure 4). This is corroborated by the snowmelt at the IMB thermistors (Figure 2d) and at the ablations stakes in the view of UW webcams (Figure 3), which indicated all snow had already melted by 6 July.

After 17 July, the reported surface position by IMB 2012C was unreliable since it was affected by the ablation shield. The readings from the ablation stakes visible in UW webcams (not shown) indicated that the ice surface after 17 July had reached maximum surface ice melt of 0.35 ± 0.05 m by early August (Figure 4), and increased by about 0.10 m due to snow accumulation on 20 August.

The ice thickness evolution shows bottom growth of 0.1 m from April to early June, and afterward, no bottom freezing or melting occurred until 18 June (Figure 4). Around 18 June, bottom melt started, but it was negligible until 14 July. The rate of bottom melt averaged nearly 0.01 m d^{-1} between 14 July and 21 August, when ice thickness decreased rapidly (Figure 4), and total of 0.38 m of bottom melt had occurred by 21 August. Thereafter, the melt rate decreased significantly, and by 14 October 0.11 m of additional bottom melt had taken place, corresponding to a rate of 0.002 m d^{-1}. Taking into account the surface melt, the ice thickness was about 1.4 m when the snow started to melt, 1.3 m when the snow had disappeared, and reached a minimum of 0.6–0.7 m in early August. Some caution must be taken when using these values, since the ice-bottom changes are taken from IMB 2012B, which was installed on thicker ice.

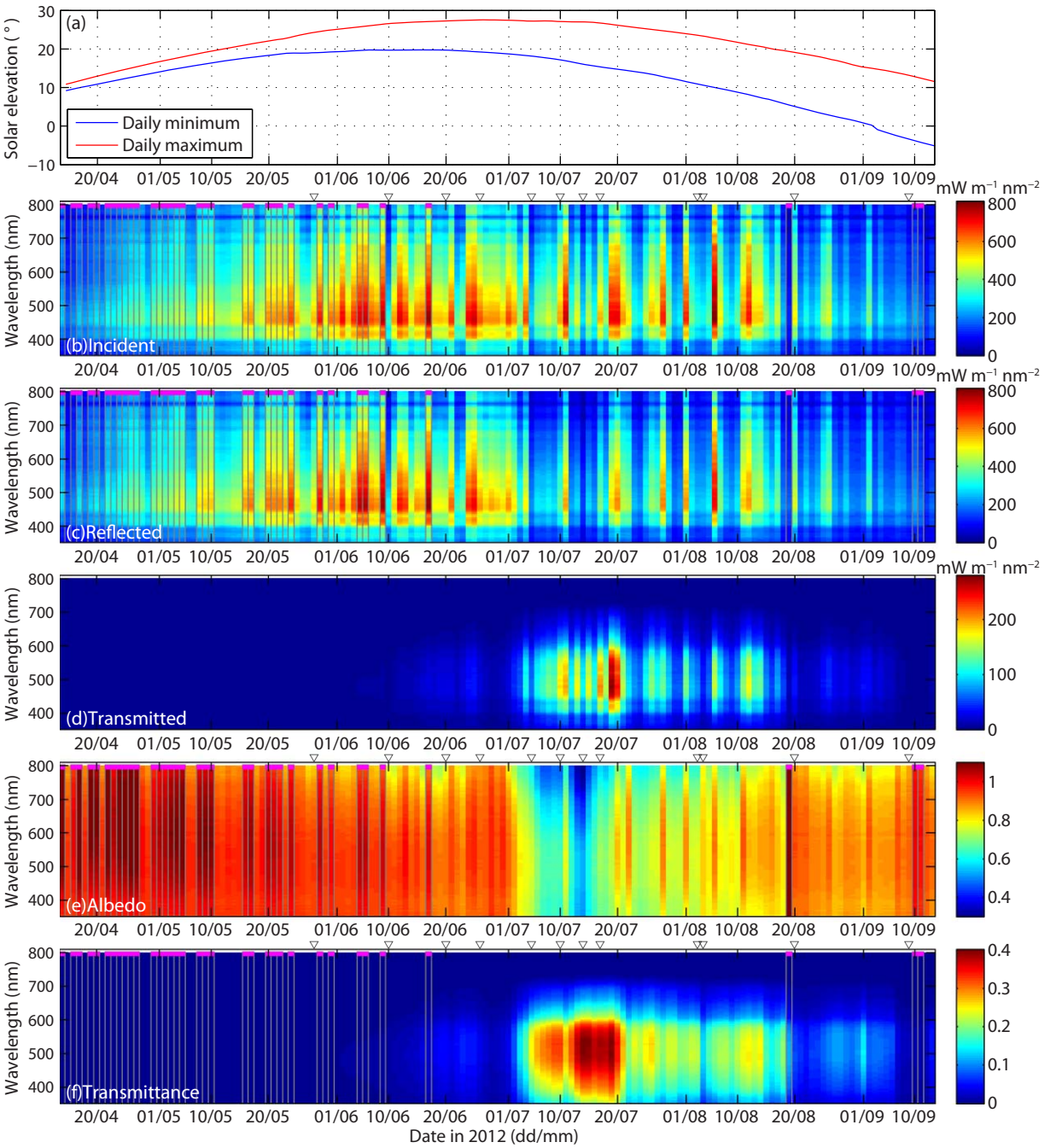

Figure 5. Time series of (a) daily minimum and maximum solar elevation angles, spectral (b) incident, (c) reflected and (d) transmitted irradiance, and spectral (e) albedo and (f) transmittance. One spectrum is shown per day from the observation at the highest solar elevation angle. Spectra containing reflected irradiance larger than the incident at any wavelength are outlined with vertical lines and marked with magenta at the top of the spectrum. As discussed in section 5.5, their values likely exceed 1 because of ice or water collecting on the incident sensor; this will not affect the transmitted fluxes. Dates shown in Figure 6 are marked with ▽ at the top of the incident, albedo, and transmittance spectra.

3.5. Seasonal Variation of Incident, Reflected, and Transmitted Spectral Irradiances

Due to the high latitude, the solar elevation at the Barneo ice floe was below 28° for the whole observation period (Figure 5a). It initially increased as the solstice approached and the ice floe drifted south; the southward drift delayed and slowed the postsolstice decrease. The highest solar elevation was above 20° between 11 May (at 88° N) and 13 August (at 83° N) and above 15° between 4 May and 1 September. The spectral incident, reflected, and transmitted irradiances at local noon and the corresponding albedo and transmittance are shown in Figures 5b–5f.

Table 2. Monthly Mean Incident, Reflected, and Transmitted In-Band (350–800 nm) Fluxes (W m^{-2}), Mean Incident and Transmitted Downwelling PAR (μmol m^{-2} s^{-1}), and Mean In-Band Albedo and Transmittance[a]

	14–30 April	May	June	July	August	1–13 September (Transmitted, 1–30)
Incident in-band, noon	95 (X/109)	161 (142/158/182)	195 (205/195/187)	152 (154/162/143)	128 (143/149/96)	76 (83/X/X)
Reflected in-band, noon	99 (X/113)	161 (148/155/177)	183 (196/179/173)	109 (111/108/109)	109 (115/129/85)	69 (73/X/X)
Transmitted in-band, noon	0.10 (X/0.12)	0.25 (0.16/0.23/0.36)	2.7 (0.7/3.1/4.3)	26 (20/38/22)	13 (18/18/4.9)	2.7 (3.3/3.1/1.8)
Transmitted in-band, daily	0.08 (X/0.10)	0.22 (0.14/0.21/0.31)	2.4 (0.6/2.7/4.0)	20 (17/29/16)	7.9 (12/9.8/2.5)	1.1 (1.5/1.1/0.56)
Incident PAR, noon	320 (X/366)	549 (480/538/622)	670 (701/669/639)	527 (532/560/492)	442 (494/510/332)	260 (281/X/X)
Incident PAR, daily	276 (X/317)	488 (427/486/545)	595 (617/576/593)	421 (458/436/372)	254 (324/272/174)	113 (123/X/X)
Transmitted PAR, noon	0.37 (X/0.43)	0.95 (0.59/0.87/1.34)	11 (3/12/17)	104 (80/148/85)	53 (71/72/20)	11 (13/12/7)
Transmitted PAR, daily	0.31 (X/0.36)	0.83 (0.51/0.78/1.17)	10 (2/11/16)	81 (68/113/63)	31 (47/38/10)	4 (6/4/2)
Albedo in-band, noon	1.04 (X/1.04)	1.00 (1.04/0.98/0.97)	0.94 (0.96/0.92/0.93)	0.72 (0.72/0.67/0.76)	0.85 (0.80/0.87/0.88)	0.90 (0.89/X/X)
Albedo in-band, daily	1.00 (X/1.00)	0.97 (1.00/0.96/0.95)	0.92 (0.95/0.90/0.92)	0.71 (0.72/0.66/0.75)	0.83 (0.78/0.83/0.88)	0.90 (0.90/X/X)
Transmittance in-band, noon	0.001 (X/0.001)	0.002 (0.001/0.001/0.002)	0.014 (0.003/0.016/0.023)	0.17 (0.13/0.23/0.15)	0.10 (0.13/0.12/0.051)	0.036 (0.040/X/X)
Transmittance in-band, daily	0.001 (X/0.001)	0.002 (0.001/0.001/0.002)	0.014 (0.003/0.016/0.023)	0.17 (0.13/0.23/0.15)	0.11 (0.13/0.12/0.049)	0.038 (0.042/X/X)
Transmittance PAR, noon	0.001 (X/0.001)	0.002 (0.001/0.002/0.002)	0.015 (0.004/0.018/0.026)	0.20 (0.15/0.27/0.17)	0.12 (0.14/0.14/0.059)	0.042 (0.047/X/X)
Transmittance PAR, daily	0.001 (X/0.001)	0.002 (0.001/0.002/0.002)	0.016 (0.004/0.018/0.027)	0.19 (0.15/0.26/0.17)	0.12 (0.14/0.14/0.056)	0.044 (0.049/X/X)

[a]Values in parentheses are averages for days 1–10 (early), 11–20 (middle), and 21–30/31 (late) in each month; X indicates data are unavailable for the period. Averages are given both from observations at noon and from observations at all times of day (daily).

At times, the observed reflected irradiance was larger at some wavelengths than the corresponding observed incident irradiance. This happened when the surface was snow covered, having a visible albedo very close to one. The most likely cause of this problem is the accumulation of ice or water on the above-ice sensors, which would most often preferentially accumulate on the incident sensor. This is best illustrated on the several cases where a sudden albedo increase (new snowfall) is accompanied by the appearance of the problem. We have indicated days when these problems occur in Figure 5; the albedo, transmittance, and incident irradiance on these days contain larger errors than the rest of the data set. While the surface radiometers are affected by these problems at times, the under-ice irradiance is unaffected since the light field is diffuse and the bioshutter prevented fouling.

There was a general increase in the incident light levels from mid-April to early July and a decrease thereafter (Figure 5b). Superimposed on this is variability caused by atmospheric conditions [*Grenfell and Perovich*, 2008]. The monthly noon in-band incident fluxes were greatest in June (195 W m^{-2}), with peak values reaching 205 W m^{-2} in early June (Table 2). The highest solar elevation was similar in June and July (Figure 5a), which would give similar incident light levels under a clear sky. The average noon in-band incident flux in July was 152, 43, and 9 W m^{-2} lower than in June and May, respectively, suggesting greater cloudiness in July.

The reflected spectral irradiance (Figure 5c) largely demonstrates similar seasonal variability as the incident spectral irradiance. The mean (daily and noon) in-band reflected fluxes were highest in June, 161 and 183 W m^{-2}, respectively. Similar to the incident fluxes, the mean in-band reflected fluxes in July were lower than in June and May, due to both lower incident fluxes and lower albedo.

Seasonal variation of the transmitted spectral irradiance was extreme (Figure 5d). The mean in-band transmitted flux under the ice was below 1 W m^{-2} until early June (Table 2). After this, it increased to 2.7 W m^{-2} in mid-June and 4.0 W m^{-2} in late June (Table 2). The mean in-band transmitted flux continued to increase to about 30 W m^{-2} (daily mean) in the middle of July. Its daily maximum was 37 W m^{-2} on 19 July (Figure 5d). From late July onward, the in-band transmitted flux decreased. However, it was still higher than the pre-melt levels until late September (Table 2). Superimposed on the seasonality of the transmitted fluxes were frequent abrupt changes, most likely related to changes in surface conditions, such as snowfall or surface freezing, and cloud conditions.

The diurnal cycle of the transmitted fluxes was significant, in particular in July. Although the amplitude of the diurnal cycle of in-band transmitted flux was largest in July, about 15 W m^{-2}, the transmitted flux was large all day ($>$10 W m^{-2}). By contrast, the daily amplitude was small in September, only 2 W m^{-2}, with the transmitted flux mainly concentrated at daytime.

The mean incident PAR was high in May, June, and July (Table 2); the highest daily mean in June was 670 μmol m^{-2} s^{-1}. The transmitted PAR was very low in April and May, $<$1 μmol m^{-2} s^{-1}. It remained larger than 2 μmol m^{-2} s^{-1} between June and September, reaching 113 and 148 μmol m^{-2} s^{-1} in mid-July, for the noon mean and daily mean, respectively (Table 2).

3.6. Spectral Albedo and Transmittance

Surface in-band albedo (Figures 5e and 6a and Table 2) was above 0.85 until the end of June, and then decreased rapidly in the first half of July, with the lowest values observed on 14 July. On that day, the in-band albedo was 0.46. Already on 17 July it had, however, increased to 0.67. Thereafter, values were above 0.6, and by 20 August the albedo had returned nearly to premelt values (Figure 6a).

Surface albedo generally decreased with wavelength above 500 nm (Figure 6a). The decline of albedo from 500 to 800 nm was relatively weakest on 26 June and 20 August when new snow fell (Figure 4), and sharpest on 14 July when the surface albedo was lowest.

Ice transmits light mainly at wavelengths 350–700 nm (Figures 5f and 6b), meaning the in-band transmitted fluxes here are approximately equal to the total broadband transmitted fluxes. Nevertheless, the in-band transmittances reported here are higher than what would be obtained with broadband sensors since they would observe greater incident fluxes. In this waveband, the variation of transmittance with wavelength is consistent with the transmittance spectral shape in other studies [e.g., *Maykut and Grenfell*, 1975; *Nicolaus et al*., 2010a] and is due to the spectral dependence of absorption in ice and brine [*Light et al*., 2008]. In-band transmittance was low in April and May ($\sim$0.001; Table 2). Afterward, it increased in June ($\sim$0.01), and further increased until mid-July ($\sim$0.2). In late July, the transmittance decreased, but was relatively high (0.1) until mid-August. In late August, it substantially decreased, and returned to nearly premelt levels in early September. Spectral transmittance was highest on 14 July, but the in-band transmittance did not vary much between 14 and 17 July (Figure 6b).

The seasonality of PAR transmittance (which is unaffected by the wavelength limitation) is similar to that of the in-band transmittance, low in April and May, and highest in mid-July (Table 2). During the middle of July when the mean in-band transmittance was largest (0.23), the mean PAR transmittance was 0.26 (Table 2).

4. Discussion

The ice floe drifted south from 89°N to 82°N from mid-April to mid-September. The surface was covered by dry snow until snowmelt onset on 10 June. The timing of snowmelt onset was similar during the *Tara* experiment [*Nicolaus et al*., 2010a], which drifted between 86°N and 89°N. Melt onset was later than during the Surface Heat Budget of the Arctic Ocean (SHEBA) field experiment [*Perovich et al*., 2002], likely because SHEBA was farther south, between 76°N and 80°N. The amount of energy reflected to the atmosphere was greatest in June, while at SHEBA this occurred a month earlier due to earlier melt onset [*Perovich*, 2005]. The timing of melt onset is important for the biological processes in and under the ice [e.g., *Arrigo*, 2003; *Lavoie et al*., 2005; *Arrigo et al*., 2012], since only very little light is transmitted through the ice and snow during spring [*Perovich*, 2005; *Nicolaus et al*., 2013]. Immediately after snowmelt onset (10 June), more light is transmitted through the ice.

The rather abrupt decrease in albedo and increase in transmittance, in the first half of July (Figure 5), coincide with decreasing snow depth (Figure 4), underlining the importance of the snow cover on the energy balance of the sea ice and underlying ocean. In contrast, the reappearance of snow in mid-August drastically decreased the amount of transmitted energy (Figure 5).

Considerable spatial variability of the Arctic sea ice surface in summer is a well-known feature [e.g., *Perovich et al*., 2001; *Hudson et al*., 2012; *Nicolaus et al*., 2012; *Perovich and Polashenski*, 2012]. In summer 2012, in our observation area, melt ponds, with patches of snow and bare ice, appeared in early July, and melt ponds reached their maximum extent in mid-July. At the SRB site, surface albedo was lowest and transmittance was highest on 14 July (Figure 5e) when there was 0.01 m snow at the IMB site (Figure 4). Thus, we surmise that snow had completely melted on 14 July at the SRB site, 3 days earlier than at the IMB site. The spectral albedo on 14 July is higher than typical melt pond albedo [*Hanesiak et al*., 2001], but smaller than bare ice albedo [*Grenfell and Perovich*, 1984; *Ehn et al*., 2011]. However, the spectral albedo was very low ($<$0.4) during 7–16 July at longer wavelengths (700–800 nm) (Figure 5e), suggesting a melt pond was in view of the SRB. This spectrum indicates there was a mixture of melt pond and bare ice surface at the SRB site at that time. From 14 July onward, surface albedo increased (Figures 5e and 6a), even though the ice surface was melting (Figure 4). The increase of albedo could be because of pond drainage [*Nicolaus et al*., 2010b], increased freeboard [*Ehn et al*., 2011], the combination of the former, formation of a surface scattering layer on the ice surface [*Perovich*, 1996; *Ehn et al*., 2011] or rapid changes of an existing scattering layer [*Grenfell and Maykut*, 1977] when it was directly exposed to melting after the snow had disappeared.

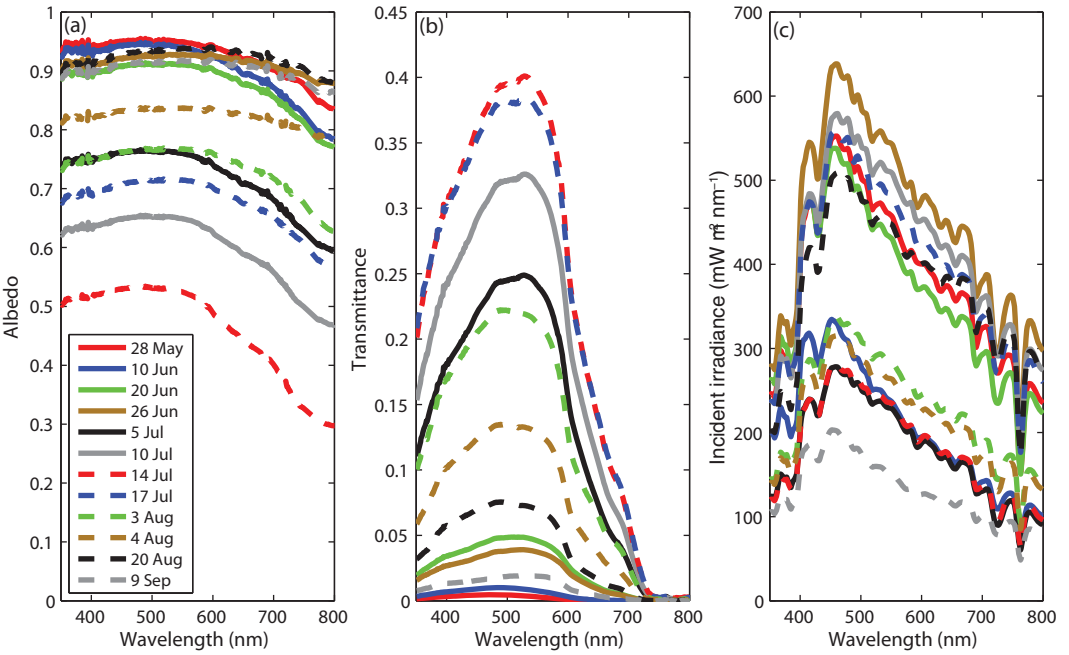

Figure 6. Evolution of spectral (a) albedo, (b) transmittance, and (c) incident irradiance from April to September 2012 on the dates indicated in Figures 5b, 5e, and 5f.

Transmittance was highest on 14 July (Figures 5f and 6b), when surface albedo was lowest (Figures 5e and 6a). Even a thin layer of new snow can reduce transmittance through the ice cover considerably [*Maykut and Grenfell*, 1975], as observed, for example, on 26 June (Figure 6b). The observation of the highest transmittance on 14 July suggests that there was no snow left on that day at the SRB site. Transmittance decreased after 14 July (Figure 5f) as the surface albedo increased. There were occasionally rapid decreases in transmitted fluxes, accompanied by rapid increases in albedo (Figures 5e and 5f). These can be explained by the formation of a thin layer of ice, e.g., on 22 July and 4 August, or the accumulation of a thin layer of new snow, e.g., on 19 August. Large reductions in the transmitted fluxes also sometimes occurred with little change to albedo or transmittance, e.g., on 24 July and 31 July, due to significantly reduced incident fluxes.

The daily transmitted energy into the ocean through the ice (Figure 7) was relatively small prior to 10 June, and increased slightly, to 0.5 MJ m^{-2} d^{-1}, later in June. In July and early August, transmitted energy values were between 1 and 3 MJ m^{-2} d^{-1}. In mid-August, values returned to below 0.5 MJ m^{-2} d^{-1} (Figure 7). From mid-April until the end of September, the accumulated energy transmitted into the ocean was 86 MJ m^{-2} (Figure 7), corresponding to 0.28 m of ice bottom melt, if all the transmitted energy was used for melt (assuming pure ice with a latent heat of fusion of 334,000 J kg^{-1} and density of 917 kg m^{-3}). This figure is just over half of the bottom melt from the IMB data (Figure 4). Transmittance through ponds, as well as through open water or leads, is much higher [*Maykut and Grenfell*, 1975]. As the IMB data are from a nearby thicker ice floe, a quantitative comparison of transmitted energy and observed melt is difficult, but if we assume the bottom melt at the SRB site was similar to the IMB site, then additional solar heating of the ocean through leads and melt ponds could easily account for the rest of the melt (at SHEBA, half of all solar energy to the ocean during the melt season entered through leads) [*Perovich*, 2005].

As noted, there was a half meter of water between the ice and the under-ice radiometer at deployment. This water layer reduces the amount of light measured at the under-ice sensor, but it is necessary to keep the radiometer initially at some distance from the underside of the ice to allow for ice growth. Correcting for light attenuation in the water layer would increase transmittance levels [*Ehn et al.*, 2011], and thereby the calculated potential ice melt. The under-ice light field in the upper ocean is highly variable in space and time and highly spatially heterogeneous and dependent on wavelength, ice thickness, and the surface conditions [*Frey et al.*, 2011; *Nicolaus et al.*, 2013]. Simply assuming isotropic radiance below the ice, and using the clear and turbid cases for radiance attenuation as observed beneath sea ice during the SHEBA experiment [*Pegau*, 2002, Table 1], we estimate that our transmitted fluxes measured 0.50–0.75 m below the ice bottom underestimate the transmitted flux right beneath the ice by 12–18% and 22–32% using the clear and turbid attenuation

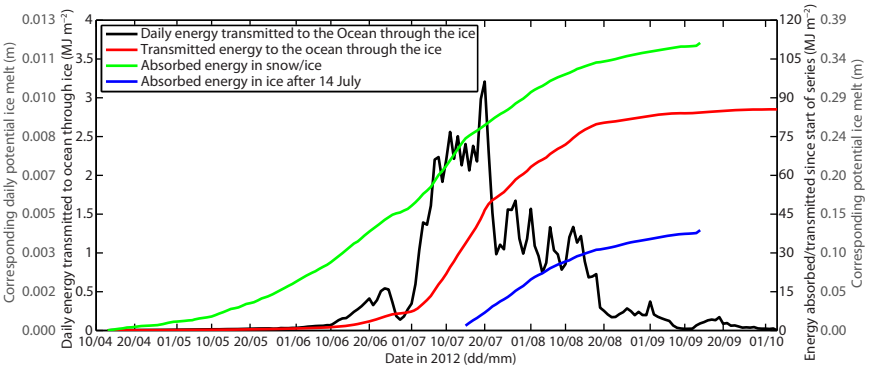

Figure 7. Daily transmitted in-band energy into the ocean through the ice (left axis, expressed in MJ m^{-2} and as equivalent melt of pure ice); cumulative energy transmitted to the ocean through the ice since start of the observations (14 April 2012, red line, right axis); cumulative energy absorbed by the snow and ice since start of the observation (green line, right axis) and cumulative energy absorbed by the ice after complete snowmelt on 14 July (blue line, right axis).

coefficients, respectively. Thus, the solar energy transmitted to the ocean through the ice likely supplied about two-thirds of the energy required for the observed bottom melt at the SRB site.

The in-band energy absorbed in the snow and ice is also shown in Figure 7. Sunlight in this wavelength band may be absorbed at the surface or within the snow and ice; the significant amount of out-of-band (unobserved) sunlight is mostly absorbed at the very surface. As previously mentioned, we believe the corrupted data indicated in Figure 5 (albedo greater than 1 at any wavelength) are due to ice or water collecting on the upward looking sensor. Removing these data would require very uncertain interpolations to perform daily or seasonal analyses; so for now we have included the entire data set, realizing that at times when the upward looking sensor was covered we are underestimating the incident radiation at the surface. Therefore, the numbers presented here for absorbed energy need to be viewed cautiously, as a likely underestimation of the true in-band absorption. Such problems appear to have happened primarily during times of snowfall, when the albedo is very high and therefore absorption is minimal. This issue does not affect the discussion of transmitted energy above since that is measured independently from the above-ice sensors.

In-band absorption was negligible until the end of May, increased somewhat in June, and rapidly increased in July following the decrease in albedo (Figure 5) and snow depth (Figure 4). Most energy was used for snowmelt before 14 July when there still was snow, and thereafter mainly for ice (surface and internal) melt. If all the absorbed in-band energy after 14 July was used for surface ice melt, the ice surface would have melted about 0.11 m (Figure 7). This value was smaller than the 0.3–0.4 m of surface melt at the stakes and thermistors. Considering the significant absorption of energy at longer wavelengths that was not observed here, and more melting visible around the ablation stakes, it seems there was more than enough solar energy absorbed to explain the observed ice surface melt.

Obtaining high quality of solar radiation partition data is challenging in polar regions without immense amount of work and logistics. The SRB setup in this study functioned reasonably well in the harsh conditions that prevailed. We observed some periods when the quality of the incident and reflected irradiance measurements were reduced, in particular from April to mid-June (outlined and marked with magenta bars in Figure 5). This was because the upward looking radiometer would likely be impacted more than the downward looking one when snow, rime, or condensation accumulated on the sensors. This is likely one of the greatest challenges in obtaining high-quality (autonomous) irradiance data in the high Arctic. To circumvent this problem, either ventilated and/or heated sensors could be used; however, such setups would require a lot of power, making such systems less desirable to deploy. A similar setup installed at the *Tara* drift [*Nicolaus et al*., 2010b] showed that the impact of snow, rime, or condensation on sensors without a glass dome was short lived. The data suggest this was true for the SRB deployment as well. With aid of ancillary data, especially webcam images, one can find the cause for possible erroneous data.

The setup of the SRB could be further improved. A GPS unit can be integrated into the SRB system to replace the installation of SVP that in this study provided accurate positions. Improving the quality of the incident irradiance measurements, through ventilation or heating, is possible, but difficult in autonomous remote applications. Two under-ice radiometers can be installed at different depths to measure change in

transmitted flux with depth and estimate the attenuation by water to correct for the distance to the ice bottom, though spatial heterogeneity makes this a challenging task. Although webcams recorded the surface conditions of the ice floe, the webcam was not close enough for capturing the specific surface conditions at the SRB site. A web camera could be integrated into the SRB setup to observe the seasonal evolution of the surface conditions at the installed sensors. Furthermore, the current SRB setup is rather expensive, mainly due to the high cost of the radiometers. This limits the production and use of SRBs in large numbers, which is necessary for observing spatial variability at all scales.

5. Summary and Conclusions

An autonomous Spectral Radiation Buoy (SRB) was successfully deployed to measure the partitioning of solar radiation (350–800 nm) incident on first-year sea ice in the high Arctic over a complete summer melt season. Compared to earlier setups [e.g., *Nicolaus et al*., 2010a], the SRB improvements consists of satellite data transfer and a bioshutter to avoid biofouling on the under-ice radiometer. The functioning of the system and the data collected demonstrate that the SRB system is suitable for autonomous and long-term observations in harsh conditions. In combination with SVP and IMBs buoys and a webcam, we were able to qualitatively and quantitatively describe the evolution of surface conditions, snow, and ice properties throughout the melt season, and examine how these are linked to the partitioning of the solar radiation incident on the ice floe.

The SRB drifted near the prime meridian from 89°N to 82°N through the Arctic Basin (Transpolar drift, Figure 2a) between mid-April and mid-September. Surface conditions played an integral role in the progression of albedo and transmittance. The surface on the SRB site was covered by dry snow until 10 June with consistently high albedo, and then by melting snow until mid-July, coincident with a drop in surface albedo and increase in transmittance and accelerated bottom ice melt. Changes in the surface scattering layer, caused by its further development after snow disappeared, increased freeboard or pond drainage likely lead to the increase in albedo with progression of surface melt. The data set presented here thus provides deeper insight into the vital role of surface properties in controlling both surface and bottom melt on Arctic sea ice as well as upper ocean heating.

The transmitted energy increased rapidly after snowmelt, and the majority of solar heat was transmitted to the ocean in July (20 W m^{-2} on average), even though incident in-band irradiance was largest in June. The observed transmitted solar energy through the ice contributed about two-thirds of the energy needed for the observed ice bottom melt. Additional heat sources, likely solar energy transmitted through melt ponds and open water, could explain the remainder of the observed bottom melt. Thus, solar heating alone could likely explain all of the observed melt in summer 2012, underlining the importance of accurately understanding the processes that affect the albedo and transmittance of sea ice that largely determine the fate of solar heat in the Arctic.

Acknowledgments

The authors are grateful to Jago Wallenschus (NPI) for participation in the installation of the instruments at Barneo. We also wish to thank Cyril Dempsey (Satlantic) for assistance with the datalogger, radiometers, and data processing, Frank Nilsen (UNIS) and the captain and crew of the RV *Lance* for the recovery of the SRB, and scientists from the University of Washington for sharing webcam photos. Tõnu Martma (TUT) is gratefully acknowledged for measuring the oxygen isotope samples. The study was supported by the Research Council of Norway through the projects "AMORA" (project 193592) and "RATHARC" (197236), and by ACCESS, a European project within the Ocean of Tomorrow call of the European Commission Seventh Framework Programme, grant 265863, and Norwegian Polar Institute and its Centre for Ice, Climate and Ecosystems (ICE).

References

Arrigo, K. R. (2003), Primary production in sea ice, in *Sea Ice—An Introduction to its Physics, Biology, Chemistry, and Geology*, edited by D. N. Thomas and G. S. Dieckmann, pp. 143–183, Blackwell Sci., Oxford, U. K.

Arrigo, K. R., et al. (2012), Massive phytoplankton blooms under Arctic sea ice, *Science*, *336*(6087), 1408, doi:10.1126/science.1215065.

Brandt, R. E., S. G. Warren, A. P. Worby, and T. C. Grenfell (2005), Surface albedo of the Antarctic sea ice zone, *J. Clim.*, *18*, 3606–3622.

Chang, G. C., and T. D. Dickey (2004), Coastal ocean optical influences on solar transmission and radiant heating rate, *J. Geophys. Res.*, *109*, C01020, doi:10.1029/2003JC001821.

Comiso, J. C., C. L. Parkinson, R. Gersten, and L. Stock (2008), Accelerated decline in the Arctic sea ice cover, *Geophys. Res. Lett.*, *35*, L01703, doi:10.1029/2007GL031972.

Ehn, J. K., C. J. Mundy, D. G. Barber, H. Hop, A. Rossnagel, and J. Stewart (2011), Impact of horizontal spreading on light propagation in melt pond covered seasonal sea ice in the Canadian Arctic, *J. Geophys. Res.*, *116*, C00G02, doi:10.1029/2010JC006908.

Frey, K. E., D. K. Perovich, and B. Light (2011), The spatial distribution of solar radiation under a melting Arctic sea ice cover, *Geophys. Res. Lett.*, *38*, L22501, doi:10.1029/2011GL049421.

Grenfell, T. C., and G. A. Maykut (1977), The optical properties of ice and snow in the Arctic Basin, *J. Glaciol.*, *18*, 445–463.

Grenfell, T. C., and D. K. Perovich (1984), Spectral albedos of sea ice and incident solar irradiance in the Southern Beaufort Sea, *J. Geophys. Res.*, *89*(C3), 3573–3680.

Grenfell, T. C., and D. K. Perovich (2008), Incident spectral irradiance in the Arctic Basin during the summer and fall, *J. Geophys. Res.*, *113*, D12117, doi:10.1029/2007JD009418.

Haas, C., A. Pfaffling, S. Hendricks, L. Rabenstein, J.-L. Etienne, and I. Rigor (2008), Reduced ice thickness in Arctic Transpolar Drift favors rapid ice retreat, *Geophys. Res. Lett.*, *35*, L17501, doi:10.1029/2008GL034457.

Hanesiak, J. M., D. G. Barber, R. A. De Abreu, and J. J. Yackel (2001), Local and regional albedo observations of Arctic first-year sea ice during melt ponding, *J. Geophys. Res.*, *106*(C1), 1005–1016.

Hansen, E., S. Gerland, M. A. Granskog, O. Pavlova, A. H. H. Renner, J. Haapala, T. B. Løyning, and M. Tschudi (2013), Thinning of Arctic sea ice observed in Fram Strait: 1990–2011, *J. Geophys. Res. Oceans*, *118*, 5202–5221, doi:10.1002/jgrc.20393.

Hudson, S. R., M. A. Granskog, T. I. Karlsen, and K. Fossan (2012), An integrated platform for observing the radiation budget of sea ice at different spatial scales, *Cold Reg. Sci. Technol.*, *82*, 14–20.

Hudson, S. R., M. A. Granskog, A. Sundfjord, A. Randelhoff, A. H. H. Renner, and D. V. Divine (2013), Energy budget of first-year Arctic sea ice in advance stages of melt, *Geophys. Res. Lett.*, *40*, 2579–2583, doi:10.1002/grl.50517.

Itoh, M., J. Inoue, K. Shimada, S. Zimmermann, T. Kikuchi, J. Hutchings, F. McLaughlin, and E. Carmack (2011), Acceleration of sea-ice melting due to transmission of solar radiation through ponded ice area in the Arctic Ocean: Results of in situ observations from icebreakers in 2006 and 2007, *Ann. Glaciol.*, *52*(57), 249–260.

Jackson, K., J. Wilkinson, T. Maksym, D. Meldrum, J. Beckers, C. Haas, and D. Mackenzie (2013), A novel and low-coast sea ice mass balance buoy, *J. Atmos. Oceanic Technol.*, *30*, 2676–2688, doi:10.1175/JTECH-D-13-00058.1.

Kwok, R., and D. A. Rothrock (2009), Decline in Arctic sea ice thickness from submarine and ICESat records: 1958–2008, *Geophys. Res. Lett.*, *36*, L15501, doi:10.1029/2009GL039035.

Lavoie, D., K. Denman, and C. Michel (2005), Modeling ice algal growth and decline in a seasonally ice-covered region of the Arctic (Resolute Passage, Canadian Archipelago), *J. Geophys. Res.*, *110*, C11009, doi:10.1029/2005JC002922.

Laxon, S. W., et al. (2013), CryoSat-2 estimates of Arctic sea ice thickness and volume, *Geophys. Res. Lett.*, *40*, 732–737, doi:10.1002/grl.50193.

Light, B., T. C. Grenfell, and D. K. Perovich (2008), Transmission and absorption of solar radiation by Arctic sea ice during the melt season, *J. Geophys. Res.*, *113*, C03023, doi:10.1029/2006JC003977.

Maslanik, J., J. Stroeve, C. Fowler, and W. Emery (2011), Distribution and trends in Arctic sea ice age through spring 2011, *Geophys. Res. Lett.*, *38*, L13502, doi:10.1029/2011GL047735.

Maslanik, J. A., C. Fowler, J. Stroeve, S. Drobot, J. Zwally, D. Yi, and W. Emery (2007), A younger, thinner Arctic ice cover: Increased potential for rapid, extensive sea-ice loss, *Geophys. Res. Lett.*, *34*, L24501, doi:10.1029/2007GL032043.

Maykut, G. A., and T. C. Grenfell (1975), The spectral distribution of light beneath first-year sea ice in the Arctic Ocean, *Limnol. Oceanogr.*, *20*(4), 554–563.

Nghiem, S. V., I. G. Rigor, D. K. Perovich, P. Clemente-Colón, J. W. Weatherly, and G. Neumann (2007), Rapid reduction of Arctic perennial sea ice, *Geophys. Res. Lett.*, *34*, L19504, doi:10.1029/2007GL031138.

Nicolaus, M., S. Gerland, S. R. Hudson, S. Hanson, J. Haapala, and D. K. Perovich (2010a), Seasonality of spectral albedo and transmittance as observed in the Arctic Transpolar Drift in 2007, *J. Geophy. Res.*, *115*, C11011, doi:10.1029/2009JC006074.

Nicolaus, M., S. R. Hudson, S. Gerland, and K. Munderloh (2010b), A modern concept for autonomous and continuous measurements of spectral albedo and transmittance of sea ice, *Cold Reg. Sci. Technol.*, *62*, 14–28, doi:10.1016/j.coldregions.2010.03.001.

Nicolaus, M., C. Katlein, J. Maslanik, and S. Hendricks (2012), Changes in Arctic sea ice results in increasing light transmittance and absorption, *Geophy. Res. Lett.*, *39*, L24501, doi:10.1029/2012GL053738.

Nicolaus, M., C. Petrich, S. R. Hudson, and M. A. Granskog (2013), Variability of light transmission through Arctic land-fast sea ice during spring, *Cryosphere*, *7*, 977–986, doi:10.5194/tc-7-977-2013.

Pegau, W. S. (2002), Inherent optical properties of central Arctic surface waters, *J. Geophys. Res.*, *107*(C10), 8035, doi:10.1029/2000JC000382.

Perovich, D. K. (1996), The optical properties of sea ice, *U. S. Cold Reg. Res. and Eng. Lab. Monogr.*, *96-1*, 33 pp., CRREL, Hanover, N. H.

Perovich, D. K. (2005), On the aggregate-scale partitioning of solar radiation in Arctic sea ice during the Surface Heat Budget of the Arctic Ocean (SHEBA) field experiments, *J. Geophys. Res.*, *110*, C03002, doi:10.1029/2004JC002512.

Perovich, D. K., and B. C. Elder (2001), Temporal evolution of Arctic sea-ice temperature, *Ann. Glaciol.*, *33*, 207–211.

Perovich, D. K., and C. Polashenski (2012), Albedo evolution of seasonal Arctic sea ice, *Geophys. Res. Lett.*, *39*, L08501, doi:10.1029/2012GL051432.

Perovich, D. K., and J. A. Richter-Menge (2006), From points to poles: Extrapolating point measurements of sea ice mass balance, *Ann. Glaciol.*, *44*, 188–192.

Perovich, D. K., G. F. Cota, G. A. Maykut, and T. C. Grenfell (1993), Biooptical observations of first-year Arctic sea ice, *Geophys. Res. Lett.*, *20*(11), 1059–1962, doi:10.1029/93GL01316.

Perovich, D. K., C. S. Roesler, and W. S. Pegau (1998), Variability in Arctic sea ice optical properties, *J. Geophys. Res.*, *103*(C1), 1193–1208.

Perovich, D. K., J. A. Richter-Menge, and W. B. Tucker III (2001), Seasonal changes in Arctic sea-ice morphology, *Ann. Glaciol.*, *33*, 171–176.

Perovich, D. K., T. C. Grenfell, B. Light, and P. V. Hobbs (2002), Seasonal evolution of the albedo of multiyear Arctic sea ice, *J. Geophys. Res.*, *107*(C10), 8044, doi:10.1029/2000JC000438.

Perovich, D. K., B. Light, H. Eicken, K. F. Jones, K. Runciman, and S. V. Nghiem (2007), Increasing solar heating of the Arctic Ocean and adjacent seas, 1979–2005: Attribution and role in the ice-albedo feedback, *J. Geophys. Res.*, *34*, L19505, doi:10.1029/2007GL031480.

Perovich, D. K., J. A. Richter-Menge, K. F. Jones, and B. Light (2008), Sunlight, water, and ice: Extreme Arctic sea ice melt during the summer of 2007, *Geophys. Res. Lett.*, *35*, L11501, doi:10.1029/2008GL034007.

Perovich, D. K., K. F. Jones, B. Light, H. Eicken, T. Markus, J. Stroeve, and R. Lindsay (2011a), Solar partitioning in a changing Arctic sea-ice cover, *Ann. Glaciol.*, *52*(57), 192–196.

Perovich, D. K., J. A. Richter-Menge, K. F. Jones, B. Light, B. C. Elder, C. M. Polashenski, D. LaRoche, T. Markus, and R. Lindsay (2011b), Arctic sea ice melt in 2008 and the role of solar heating, *Ann. Glaciol.*, *52*(57), 355–359.

Richter-Menge, J., D. K. Perovich, B. C. Elder, K. Claffey, I. Rigor, and M. Ortmeyer (2006), Ice mass balance buoys: A tool for measuring and attributing changes in the thickness of the Arctic sea ice cover, *Ann. Glaciol.*, *44*, 205–210.

Sankelo, P., J. Haapala, I. Heiler, and E. Rinne (2010), Melt pond formation and temporal evolution at the drifting station *Tara* during summer 2007, *Polar Res.*, *29*, 311–321.

Warren, S. G. (1982), Optical properties of snow, *Rev. Geophys. Space Phys.*, *20*(1), 67–89.